Engineering high energy density sodium battery anodes for improved cycling with superconcentrated ionic liquid electrolytes

Dmitrii A. Rakov[1,2], Fangfang Chen[1,2]*, Shammi A. Ferdousi[1], Hua Li[3], Thushan Pathirana[1], Alexandr N. Simonov[4], Patrick C. Howlett[1,2], Rob Atkin[3], Maria Forsyth[1,2]*

[1]Institute for Frontier Materials, Deakin University, Geelong, VIC 3217, Australia. [2]ARC Centre of Excellence for Electromaterials Science (ACES), Deakin University, Burwood, 3125, Australia. [3]School of Molecular Sciences, University of Western Australia, 35 Stirling Highway, Crawley, 6009, Australia. [4]School of Chemistry and the ARC Centre of Excellence for Electromaterials Science, Monash University, Clayton, 3800, Australia. Correspondence and request for materials should be addressed to M. F. (email: maria.forsyth@deakin.edu.au) and F. C. (email: chenf@deakin.edu.au).

Non-uniform metal deposition and dendrite formation in high density energy storage devices reduces the efficiency, safety, and life of batteries with metal anodes. Superconcentrated ionic liquid (IL) electrolytes (e.g. 1:1 IL:alkali ion) coupled with anode preconditioning at more negative potentials can completely mitigate these issues, and therefore revolutionize high density energy storage devices. However, the mechanisms by which very high salt concentration and preconditioning potential enable uniform metal deposition and prevent dendrite formation at the metal anode during cycling are poorly understood, and therefore not optimized. Here, we use

atomic-force microscopy and molecular dynamics simulations to unravel the influence of these factors on the interface chemistry in a sodium electrolyte, demonstrating how a molten salt like structure at the electrode surface results in dendrite free metal cycling at higher rates. Such a structure will support the formation of a more favorable solid electrolyte interphase (SEI) accepted as being a critical factor in stable battery cycling. This new understanding will enable engineering of efficient anode electrodes by tuning interfacial nanostructure via salt concentration and high voltage preconditioning.

The electrolyte/electrode interface and the solid electrolyte interphase layer at an alkali metal electrode in a battery is critical for performance[1,2,3,4]. The SEI consists of an insoluble passivating film on the electrode surface which prevents electrolyte decomposition whilst presenting a low resistance pathway for alkali ion transfer during deposition and stripping[3,4,5,6], and a compact, homogeneous SEI suppresses dendrite formation[3,4,5,6]. The composition and morphology of the SEI is controlled by the arrangement and chemical species of various ions or solvent molecules at the interface (also called interfacial nanostructure)[3,4,5,6]. However, a thorough understanding of the electrified interface in any electrolyte/electrode system, and the criteria for optimization of the SEI, remain unknown.

Ionic liquids (ILs)[1,7] are pure salts in a liquid state. The strong forces between IL ions (electrostatic, hydrogen bonding, van der Waals, etc), means ILs typically assemble into well-formed interfacial layers near solid surfaces that can extend a few nanometers into solution[1,8]. For pure ILs at electrode surfaces, application of an electrostatic potential significantly enhances the interfacial IL structure, leading to more and well-defined layers, as revealed by *in situ* surface-characterization techniques, including atomic force microscopy (AFM)[9,10,11], surface force apparatus (SFA)[12], scanning tunneling microscopy

(STM)[13,14], infrared reflection spectroscopy[15,16], Raman spectroscopy[17,18], sum frequency generation spectroscopy (SFG)[19], and molecular dynamics (MD) simulations[9,10,20]. The interfacial nanostructures were demonstrated to link to electrochemical performance of an IL/metal anode systems[21,22,23]; the IL cation and anion chemistry was also found to have a dramatic effect on interfacial layering near the electrode surface[9,10,21,24,25]. The effect of salt concentration on interfacial nanostructures was also considered but with a focus on low to moderate salt concentration range[26,27,28]. From several recent studies[29,30,31,32], we know that dendrite free metal anode cycling is possible in so-called '*superconcentrated*' IL electrolytes (e.g. 1:1 ratio IL to Li or Na salt) even at high rates, whereas the contribution and role of the interfacial nanostructure in these systems towards the reported enhanced cycling is yet to be established.

Here, we investigate the effect of sodium bis(fluorosulfonyl)imide (NaFSI) salt concentration and applied potential on the interfacial structure and composition of an IL *N*-methyl-*N*-propyl pyrrolidinium bis(fluorosulfonyl)imide (C3mpyrFSI) (Supplementary Fig. 1) at a negatively charged metal electrode. We suggest a novel engineering strategy for the formation of a uniform interfacial electrolyte structure dominated by $Na_x(FSI)_y$ clusters and the exclusion of organic IL cation. This has multiple important effects: firstly, avoiding parasitic reduction of the organic cation (eg. pyrrolidinium in this case) that leads to a poorer SEI layer[5,6]; secondly, a more facile reduction of the $[FSI]^-$ anion which can subsequently form a more uniform inorganic NaF layer; and finally, a significantly higher interfacial Na^+ ion concentration supporting homogeneous metal deposition. The inorganic fluorides have been identified both in Li metal and Na metal anodes as important components of SEI layers for alkali metal anode batteries[5,6,33,34].

Atomic force microscopy (AFM) measurements were performed to examine the interfacial nanostructure of C3mpyrFSI adjacent to a gold electrode at open circuit potential (OCP)

and OCP-0.5 V, focusing on the effect of low and high NaFSI salt concentrations and applied potential (for details, see Methods and Electronic Supplementary Information). The AFM force–distance profiles for C3mpyrFSI with 0, 10 and 50 mol% of NaFSI salt presented in Fig.1a-f indicate a multi-layer IL interfacial nanostructure within 4.5 Å of the gold electrode that attenuates in the bulk phase, consistent with previous reports[9,10,24,25]. A series of pronounced, discrete steps are evident which are due to the repulsive interaction from the AFM cantilever required to rupture the interfacial layers. The intensity of force is reflected from the maximum of each step and the larger force is normally related to the higher degree of ordering due to the stronger cohesive interactions in the ion layer.

The distinct effect on interfacial layering nanostructure from NaFSI concentration has been captured here. Compared to the force-distance profile of the neat IL at OCP in Fig. 1a, the 10 mol% salt system in Fig. 1b shows a similar number of 4 - 5 steps, but these become more pronounced, reflected as an increase in height. This indicates the rupture force required to break each layer is enhanced in the 10 mol% system due to the strengthening in ion-ion association. Further addition of NaFSI salt to 50 mol% significantly changes the interfacial structure compared to that of 0 and 10 mol% systems, with only 2 or 3 steps remaining along with a large decrease in the rupture force. Furthermore, the different concentrations also shift the position of the discrete steps, therefore, indicating a change in physical dimensions of interfacial ion packing.

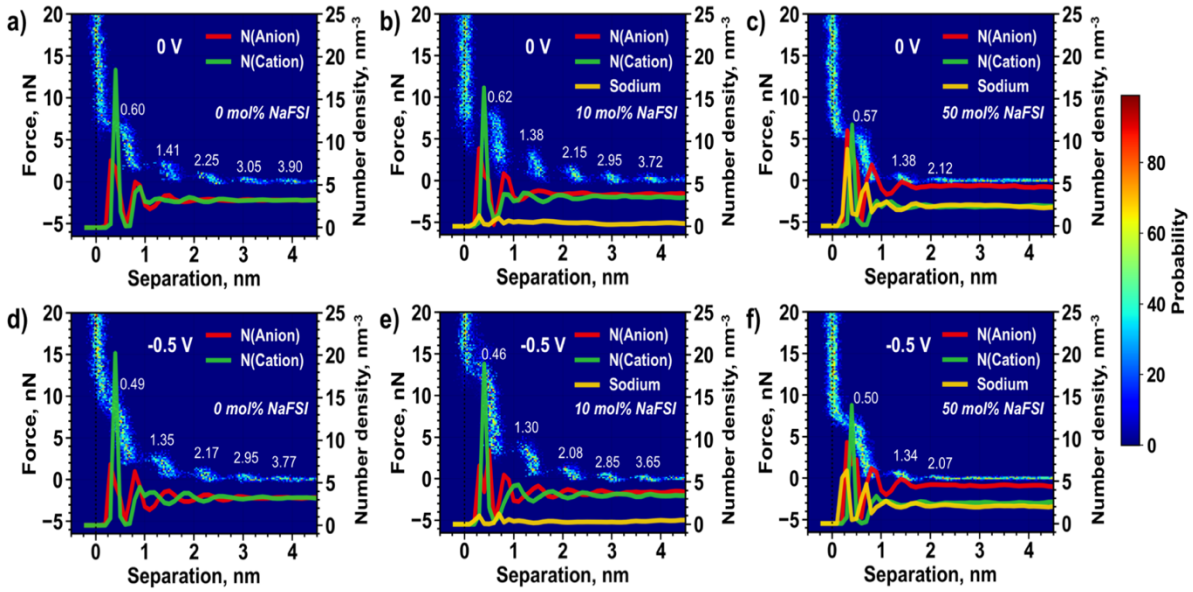

Fig. 1 | Experimental AFM force-distance 2D histograms and ion number densities derived from MD simulations (*red* – $[FSI]^-$, *green* – $[C3mpyr]^+$, *yellow* – Na^+) at OCP and PZC for C3mpyrFSI with different NaFSI salt concentrations of (a) 0 mol%, (b) 10 mol%, (c) 50 mol% near Au(111) electrode. AFM force-distance 2D histograms and MD ion number densities obtained at OCP-0.5 V and -0.5 V vs. PZC for C3mpyrFSI with different NaFSI salt concentrations of d) 0 mol%, e) 10 mol%, f) 50 mol% near Au(111) electrode.

Disruption of the IL interfacial layered structure by high salt concentration correlates with the increase in the number of Na^+ at the interface, which alters the chemical composition of the inner electrolyte layers. Similar observations were also reported in previous works on *N*-butyl- *N*-methylpyrrolidinium ($[C4mpyr]^+$) cation based ILs with either Li or Na salt (up to 1 M)[26,27,28]. However, the results here for the Na salt and the smaller $[C3mpyr]^+$ cation show some distinct differences, likely related to the effect of the shorter alkyl substituent on packing and surface organization. The effect of cation structure on IL interfacial organization was demonstrated previously by Begic et at[21].

The change in AFM force-distance profiles due to increased salt concentration is also evident when -0.5 V is applied to the working electrode (Fig. 1d-f). When comparing the

structure at open circuit potential (OCP) relative to OCP-0.5 V, we see that this level of applied negative potential has a negligible effect on the number of ion layers for a given system, however, it displaces the AFM steps closer to the electrode surface and also increases rupture forces, and this is particularly evident for the 0 and 10 mol% salt systems. In order to gain further insight into the impact from salt concentration on interfacial nanostructures, we conducted atomistic molecular dynamics (MD) simulations on an ideal interface model consisting of IL electrolytes with different Na salt concentrations that are confined between two flat Au(111) electrodes at potential of zero charge (PZC), -0.5, and -1.25 V vs. PZC. Ion number density profiles of both cation, anion (generated through the Nitrogen atom) and the Na ion at PZC and -0.5 V vs. PZC are also presented in Fig. 1. For the 0 and 10 mol% salt systems, the number density profiles show around 5 and 5-6 peaks, respectively, and this agrees well with the AFM results. The number of peaks in the density profiles of both cations and anions reduces to 3 as the salt concentration increases to 50 mol% and this again reproduces the change observed in the AFM measurements. Furthermore, the height of the first sharp peak for the IL cation reduces with increased salt concentration whereas that of both anion and Na^+ increases, suggesting the growth in the number of both $[FSI]^-$ and Na^+ ions in the innermost layer at higher salt concentration. It is noticed here that the position of the first AFM step (between 2 and 9 Å) is related to the first two peaks in the density profiles. The positions of other AFM steps match with peaks of the anion density profiles better than that of cations. This means that more force is required to displace the anions than the cations, which can be a consequence of the anion heavier than $[C3mpyr]^+$ (molecular mass in g mol^{-1}: $[FSI]^-$ (180.12) > $[C3mpyr]^+$ (128.23))[10]. Furthermore, the possible effect from water traces on interfacial nanostructure was also investigated via MD simulations, and no significant change on both position and number of density peaks was found (Supplementary Fig. 2).

To reveal the molecular origin of the experimentally detected ionic layers, we divided the simulation box adjacent to the negatively charged electrode surface into three regions, covering the Z-distances of 0-0.61, 0.61-1.1 and 1.1-1.85 nm, respectively, and calculated the radial distribution function (RDF) of Na-FSI within these three regions (Supplementary Fig. 3). The RDF curves clearly demonstrate a decrease in Na-FSI structural order at a Z-distance farther away from the electrode, which is supported by the attenuated AFM steps shown in Fig. 1. This is also consistent with previously reported experimental observations[8,10,11,26,28,35]. In general, the coordination number (CN) of Na-FSI of the 50 mol% system is higher than that of 10 mol% system, and the difference in CN becomes even larger at -0.5 V vs. PZC. The increased CN of Na-FSI coordination is also reported in the bulk phase simulation of this IL at the higher NaFSI salt concentrations, which was suggested to be a consequence of the formation of extended $Na_x(FSI)_y$ ion aggregates[36]. The increase in Na-FSI coordination number not only results in a decrease in binding strength between Na^+ and $[FSI]^-$ due to enlarged anion repulsive energy[30,31,36,37,38,39], but also promotes the local dynamics of $[FSI]^-$ in the 50 mol% system, and consequently enhances the Na ion hopping events demonstrated as a more frequent change in the number of Na^+ counted in the innermost layer (Supplementary Fig. 4) near the electrode.

To further analyse the chemical composition of the innermost interfacial layer in relation to the salt concentration and applied electrode polarization, the cation/anion ratio and the number of Na^+ at all simulated potentials are plotted in Fig. 2. The presence of cations, anions and sodium ions is not only affected by salt concentrations, but also responds differently to applied electrode potentials. In the neat IL and low salt concentration systems, the $[C3mpyr]^+/[FSI]^-$ ratio increases with increasingly negative applied potential. This demonstrates that the increased negative charge on the electrode enriches pyrrolidinium cations in the innermost layer to screen the excess negative surface charge

(Supplementary Table 3, Supplementary Fig. 5). In contrast, this ratio changes oppositely in the 50 mol% salt system, decreasing from 0.60 to 0.33 as the potential is changed from -0.5 V to -1.25 V vs. PZC. This is a result of the partial exclusion of IL cations and a concomitant increase in anions. Additionally, the number of Na^+ significantly increases in in the innermost layer at -1.25 V compared to PZC or even -0.5 V (Fig. 2b). There is thus a competition between $[C3mpyr]^+$ and Na^+ entering the innermost layer to compensate the negative charge on the electrode; an increase of the former will reduce the number of both Na^+ and $[FSI]^-$ ions whereas an increase in Na^+ brings accompanying $[FSI]^-$ anions to satisfy the coordination of the alkali metal cation. The smaller Na^+ more readily fills the free space in the innermost layer compared to the bulky $[C3mpyr]^+$, consequently, providing sufficient positive charges to screen the negatively charged surface. This also reduces the layered nanostructuring at the interface compared to the more extensive layering found in the case of 0 and 10 mol% systems that can be caused by inefficient surface charge screening due to poor packing of the bulky cations[26,27,28].

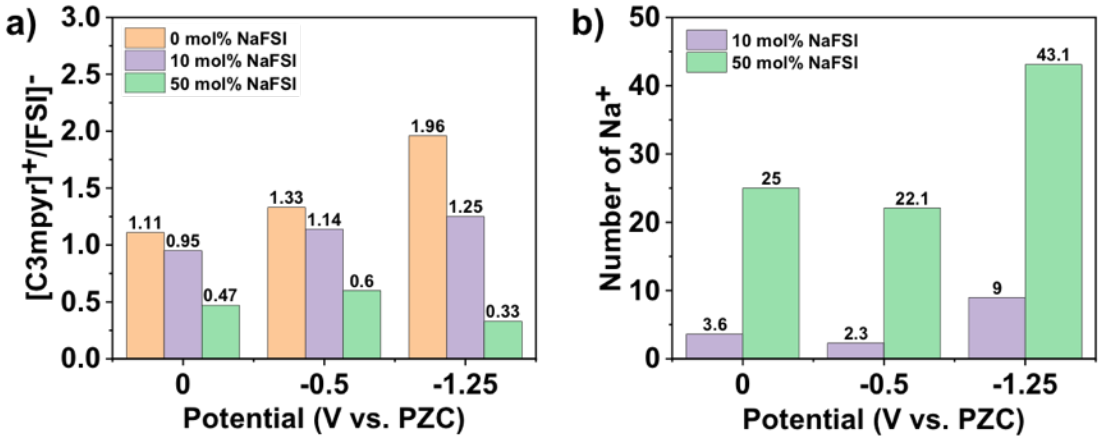

Fig. 2 | (a) Number ratio of $[C3mpyr]^+/[FSI]^-$ and (b) number of Na^+ in the innermost layer at the Au(111) electrode surface at PZC, -0.5 V, and -1.25 V vs PZC.

The angular distribution analysis of inner layer $[C3mpyr]^+$ shows that the pyrrolidinium ring tends to align parallel to the gold surface (Supplementary Fig. 6). In addition, the

subsequent decrease in the vertical orientation at the negative potential provides further insight for the first AFM layer contraction found in Fig. 1 at OCP-0.5 V.

The co-existence of Na^+ with $[FSI]^-$ in the inner layer is another characteristic in these systems. In previous studies considering salt concentration (e.g. < 0.5 M), the Na^+ is normally solvated by 2-3 $[FSI]^-$ anions[26]. Meanwhile, here our interest is in the superconcentrated IL electrolytes that demonstrate superior battery performance[30,31,40,41]. In this case, the $Na_x(FSI)_y$ ion aggregation becomes more obvious and extensive. The Na-FSI coordination structures are the same as those found in the bulk phase[36] which are denoted by A_1 (Na^+ coordinates to the N atom), A_2 (bi-dentate, Na^+ coordinates to oxygen atoms on both sides of the N atom) and A_3 (mono-dentate, Na^+ coordinates to oxygen atoms on one side of the N atom) on three RDF peaks between 0.2 and 0.6 nm in Fig. 3. The peaks change differently between low and high salt concentration systems in particular as the applied potential changes. In the 10 mol% system in Fig. 3a, the A_2 Na-FSI coordination dominates when the electrode becomes more negatively charged. This is accompanied by a decrease in Na-FSI coordination number (CN) mainly relating to the decreased A_3 coordination. However, in the case of the 50 mol% system, the A_2 coordination only increases slightly from PZC to -0.5 V vs. PZC and then sharply decreases at -1.25 V vs. PZC as A_3 coordination becomes prevalent. The increase in A_3 and CN is a result of the formation of large molten salt like $Na_x(FSI)_y$ ion aggregates (Fig. 3d), which has been also reported in the bulk IL phase with higher salt concentrations[36]. The A_2 structure has a higher binding energy than the A_3 structure[42,43] and thus is more difficult to break, this is consistent with the higher rupture force found in the AFM studies for the 10 mol% system compared to the 50 mol% system.

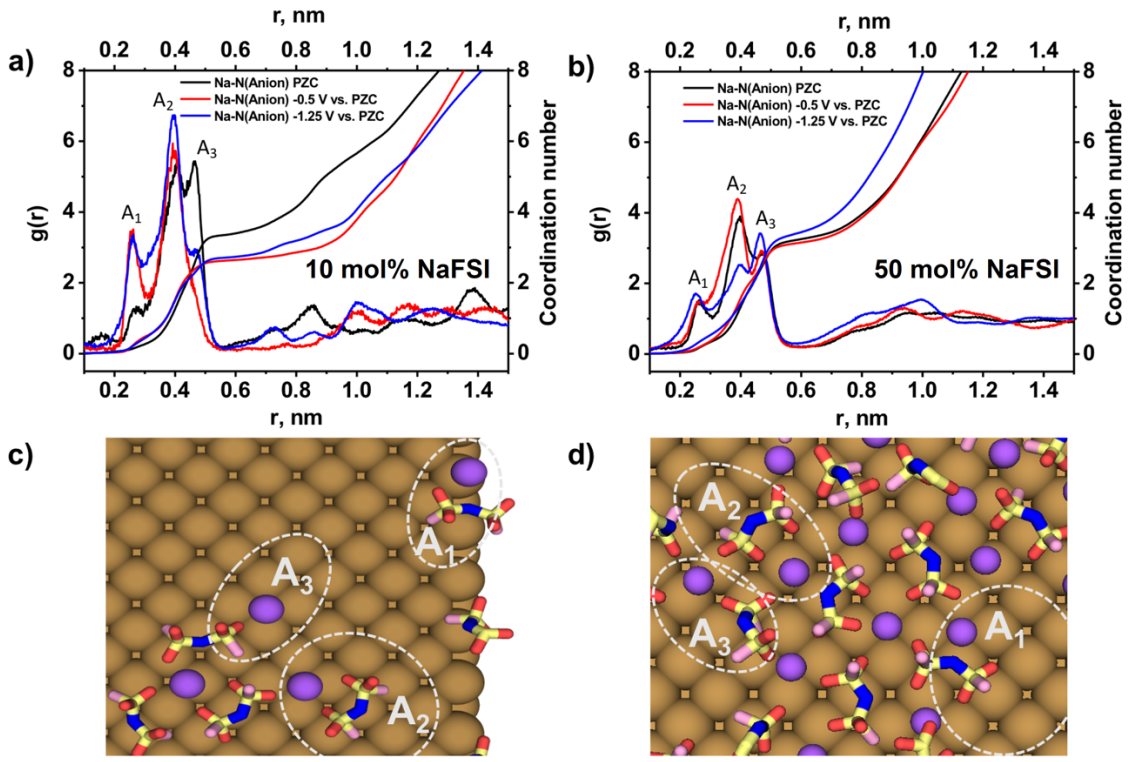

Fig. 3 | Radial distribution function g(r) and coordination number calculated for Na-N_{FSI} coordination in the innermost layer within 0.61 nm of the electrode surface for (a) 10 mol% and (b) 50 mol% salt systems. Two snapshots show typical $Na_x(FSI)_y$ complexes in the innermost layer at -1.25 V vs. PZC in the (c) 10 mol% and (d) 50 mol% salt systems; three types of Na-FSI coordination: A_1, A_2 and A_3 are highlighted.

These simulation results also provide an insight into the underlying reason of the commonly observed improved electrochemical cycling behavior, the uniform morphology of metal anode surface, and/or the low-charge transfer resistance (R_{ct}) reported in superconcentrated ILs[29,30,31]. The existence of the extended highly coordinated $Na_x(FSI)_y$ aggregates at the electrified interface can lead to a higher nucleation rate for Na metal deposition resulting from the dominance of the Na^+ ions and their likely higher diffusivity in these molten salt like IL electrolyte structures; previous MD simulations on the same IL, for example, showed that the Na^+ ion transport is faster in the 90 mol% NaFSI system due to facilitated reorganization and exchange of the coordination environment[36]. In addition,

the uniform distribution of the $[FSI]^-$ near the anode surface and the expulsion of the $[C3mpyr]^+$ from the innermost layer contributes to the formation of more uniform and homogeneous SEI layer from the decomposition of $[FSI]^-$ to form NaF, favoring a more stable cycling[6,33,44]. Of further significance with respect to SEI layer design is that the 50 mol% system tends to form a molten salt like $Na_x(FSI)_y$ aggregate interfacial structure when a higher negative potential is applied, whereas the low salt concentration (10 mol%) system does not. This indicates that not only the use of high salt concentration in IL[30,31] but also applying a high voltage pre-treatment could optimize interfacial chemistry and improve the electrochemical performance of the battery.

In order to test this hypothesis, we applied different negative electrode polarizations, in an experimental system based on the 50 mol% C3mpyrFSI IL as a precondition treatment before electrochemical cycling in a Na symmetric cell at 50 °C. The different electrode polarizations were realized through applying three different current densities of 0.1 $mAcm^{-2}$, 1.0 $mAcm^{-2}$, and 5.0 $mAcm^{-2}$, respectively for 5 brief cycles (0.1 mAh cm^{-2} per step) on three samples; the higher current density leads to the higher polarization potentials. Each of these samples was further cycled at different current densities of 0.1 $mAcm^{-2}$ and 1.0 $mAcm^{-2}$, for longer duration cycles (0.1 and 1.0 mAh cm^{-2} per step) of 20 cycles each. The chronopotentiometry voltage profiles are given in Fig. 4 (Supplementary Fig. 7). It is clear that the preconditioning at 5.0 $mAcm^{-2}$ leads to the largest initial polarization potential and the shortest deposition time (for an equivalent amount of charge), however, for the subsequent cycling at both 0.1 $mAcm^{-2}$ and 1.0 $mAcm^{-2}$ this cell shows the smallest overpotential among the three cells. The electrochemical impedance spectra obtained after 20 cycles at 0.1 $mAcm^{-2}$ confirms the formation of a lower R_{ct} surface for the cell preconditioned with a high current density (Fig. 4c). Further cycling at 1.0 $mAcm^{-2}$ and 5.0

$mAcm^{-2}$ also demonstrates that preconditioning at high current density favorably contributes to symmetric cell cycling behavior at even higher rates, while the other two cells preconditioned at lower currents (0.1 $mAcm^{-2}$ and 1.0 $mAcm^{-2}$) either fail due to short circuiting or exhibit unstable voltage profiles. In prior work, similar observations were reported for the cycling of a symmetric Na cell with a solid state electrolyte based on a 90% NaFSI salt in a phosphonium IL (methyl triisobutyl phosphonium FSI). In that work it was also demonstrated that initial preconditioning of Na at higher current density lead to lower polarization potential for subsequent cycling as observed here[45] without giving any explanation for this phenomenon. In this work we now have a clear understanding towards the influence of the preconditioning voltage (as applied through deposition at higher current density) on interfacial structuring near a negatively charged electrode and can infer from this the positive formation of a favorable metal anode surface (SEI and/or uniform morphology of anode surface). Very recently, we have also experimentally demonstrated a similar effect for lithium metal anodes in an equivalent superconcentrated LiFSI electrolyte (C3mpyrFSI with 50 mol% LiFSI) where, compared to deposition at 1.0 $mAcm^{-2}$, higher average cycling efficiency, more uniformed deposition and suppression of dendrite growth was accompanied by the presence of a thinner, LiF dominated SEI layer (as shown by XPS and ToF-SIMS surface analysis) upon deposition at high current densities of 20 $mAcm^{-2}$; deposition voltages in this case were more negative than -0.6 V vs Li[34].

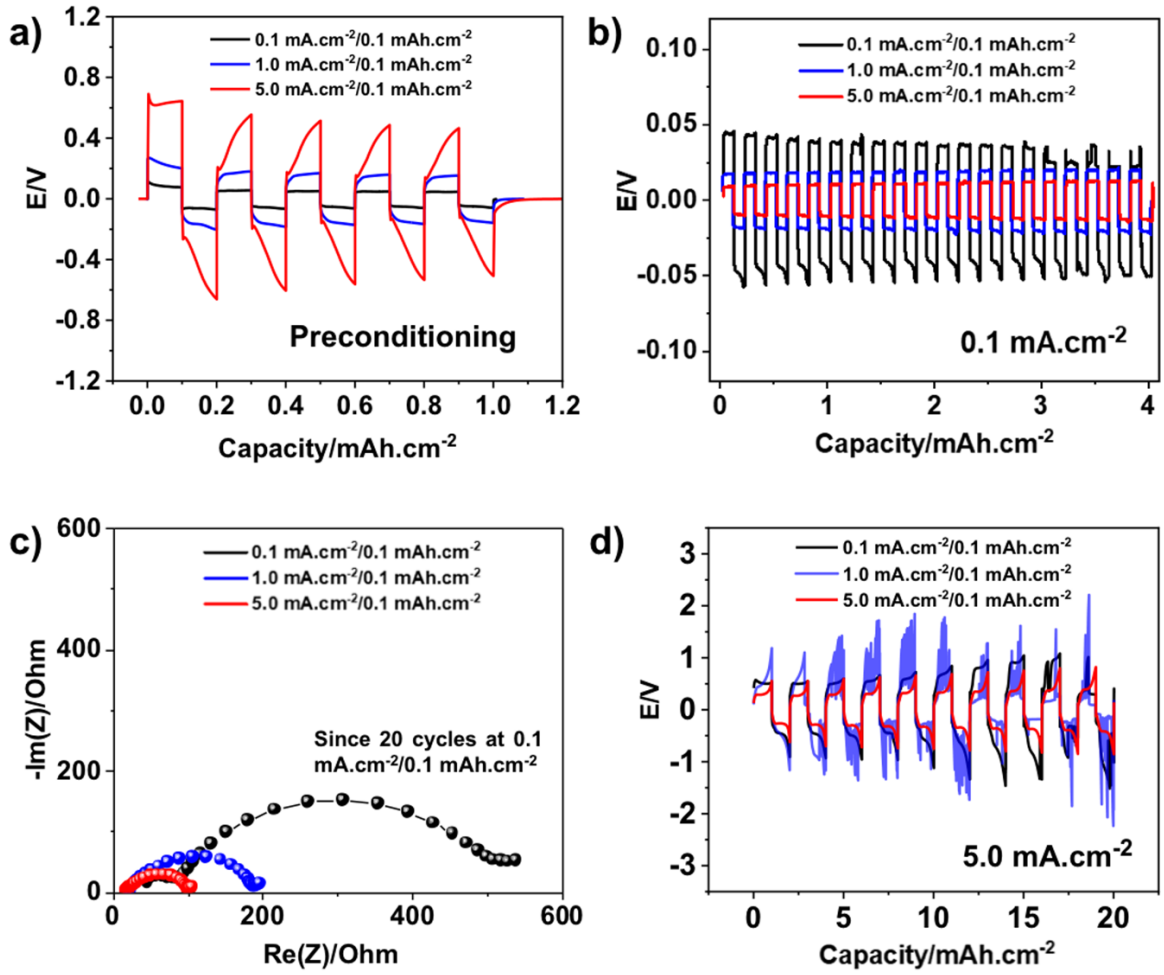

Fig. 4 | (a) The cells preconditioning at 0.1 mAcm^{-2}/0.1 mAhcm^{-2} (*black*), 1.0 mAcm^{-2}/0.1 mAhcm^{-2} (*blue*), and 5.0 mAcm^{-2}/0.1 mAhcm^{-2} (*red*) within 5 cycles. (b) Galvanostatic stripping-plating cycling of Na|50 mol% NaFSI in C3mpyrFSI|Na cell at 50 °C at 0.1 mAcm^{-2}/0.1 mAhcm^{-2}. (c) Nyquist plot recorded for the cells after 20 cycles at 0.1 mAcm^{-2}/0.1 mAhcm^{-2}. (b) Galvanostatic stripping-plating cycling of Na|50 mol% NaFSI in C3mpyrFSI|Na cell at 50 °C at 5.0 mAcm^{-2}/1.0 mAhcm^{-2}.

In conclusion, by means of AFM and MD simulation, it is found that a superconcentrated C3mpyrFSI IL electrolyte with 50 mol% NaFSI has a dramatically different interfacial structure from that of a neat IL or its low salt concentration counterpart. A highly aggregated $Na_x(FSI)_y$ structure, reminiscent of the molten salt like structure previously

reported for the bulk phase[36] is found in the innermost electrolyte layers, in particular at a negatively electrified surface, that disrupts the interfacial nanostructuring as observed from the significantly reduced number of steps in AFM force-distance profiles. The interfacial structure in superconcentrated IL electrolytes can be further optimized through adopting a high voltage pre-treatment, that promotes the formation of an even higher concentration of $Na_x(FSI)_y$ aggregates on the negative electrode and also excludes the $[C3mpyr]^+$ cations. The hypothesis that such structures lead to improved SEI layer and metal deposition was confirmed by the demonstration of significantly improved electrochemical performance of a superconcentrated C3mpyrFSI|NaFSI cell which was preconditioned with a high current density protocol before further cycling. This work, for the first time, clearly discloses the mechanism of improved cycling stability in superconcentrated IL electrolytes with respect to the electrolyte structure at an electrified anode, and provides insights for rational electrolyte design and engineering of metal anode surfaces for high energy density, high-performance batteries with long cycle life.

Methods Materials

N-methyl-*N*-propylpyrrolidinium bis(fluorosulfonyl)imide (C3mpyrFSI, 99.9%) and sodium bis(fluorosulfonyl)imide (NaFSI, 99.99%) were obtained from Solvionic and used without further purification. The NaFSI salt contained electrolytes were prepared by dissolving the salt in C3mpyrFSI in argon-atmosphere glove box with further heating at 50 °C for 24 h. The water content in these electrolytes was measured by coulometric Karl Fischer method (831 Karl Fisher Coulometer with Hydranal® Coulomat AG as the titrant), and does not exceed 55 ppm. All samples for electrochemical measurements were kept inside argon-atmosphere glove box.

Electrochemical experiments

Symmetrical Na|Na CR2032 Hoshen coin cells were fabricated with two sodium metal

electrodes (Sigma-Aldrich, purity 99.9%), which were stored in paraffin oil (Merck Millipore). Inside an argon filled glove box, sodium electrodes (8 mm diameter) were prepared by removing paraffin oil traces with dried n-hexane, followed by rolling, brushing and punching. A ½ inch (12.7 mm) diameter polyethylene separator (gratis, Lydall, 7P03A, 50 μm thickness, 85% 0.3 μm porosity) soaked with the electrolyte solution was used. Two spacers of 0.5 mm and 1.4 mm spring were used to ensure contact. After sodium symmetrical cell preparation and resting for 24 hours at 50°C, electrochemical impedance spectroscopy (EIS) was used to monitor changes on the sodium electrode surface. The EIS spectra were recorded by a multi Potentiostat VMP3 (Bio-Logic) in a frequency range of 50 mHz to 1 MHz with a 10 mV voltage amplitude. The result was analysed by using EC-Lab software (Z Fit V. 10.44). These cells were cycled using chronopotentiometry mode with various current densities being applied at 50 ^{0}C (20 cycles at 0.1 mAcm^{-2}/0.1 mAhcm^{-2}, 1.0 mAcm^{-2}/1.0 mAhcm^{-2}, and 10 cycles at 5.0 mAcm^{-2}/1.0 mAhcm^{-2}) from low current to high current densities. Prior to 20 chronopotentiometric cycles, each cell was preconditioned at three different current densities at 50 ^{0}C (5 cycles at 0.1, 1.0, 5.0 mAcm^{-2}) with amount of charge of 0.1 mAhcm^{-2}.

Molecular dynamic simulation

The all-atom classic molecular dynamic simulations were conducted with customized GROMACS software package[46]. The Canongia Lopes-Padua (CL&P) force field parameters were used in this work for C3mpyrFSI ionic liquids, which we also adopted previously for bulk phase investigation of the same IL[36]. The Lennard-Jones potential parameters (ε=22.1333 kJ/mol and σ=0.2629 nm) for Au electrode were adopted from literature[47], which were previously validated for pyrrolidinium-based IL/Au(111) interface structure analysis.

The bulk phase densities of all systems (Supplementary Table 1) were calculated first and

the computational details are described in supplementary file. The interface models were constructed with the IL electrolytes confined between two Au(111) face-centred cubic electrodes (Supplementary Fig. 1). The simulation box consisting of electrode and electrolytes has the x and y dimension according to the size of gold electrode, and the z-length was calculated based on the bulk phase density of ILs. An extra vacuum space twice the length of electrolyte was also introduced outside one side of electrode in order to eliminate the artefact images resulting from the simulation in slab geometry[1]. An annealing process was simulated at first by changing temperature from 393 K to 700 K and to 393 K again before a long equilibration calculation at 393 K for a total of 12 ns using an NVT ensemble and the Nose-Hoover thermostat. The annealing procedure allows the system to gain sufficient dynamics to obtain a reasonable initial structure for equilibration calculation. Both energies and pressures were checked to determine whether the system reaches the equilibrium. An additional 40 ns production run were performed at 393 K for structural and dynamics analysis. The trajectory file was written every 2 ps. The electrode potential was determined according to Poisson equation[11,20,47,48], by calculating the electric double layer (EDL) potential drop between two electrodes $U_{EDL} = \psi_{electrode-}\psi_{bulk}$. The U_{EDL} for uncharged electrode was defined as potential zero charge (PZC). The electrode potential -0.5 and -1.25 V vs. PZC is defined as $U_{EDL} = \psi_{electrode-}\psi_{bulk} - PZC$. The surface charges used to achieve the electrode potential are given in Supplementary Table 2.

Atomic force microscopy measurements

Atomic force microscopy (AFM) measurements were conducted on a Bruker Nanoscope Ⅳ multimode instrument operating in contact mode. The ILs were syringed into a AFM liquid cell, where the IL was isolated from the atmosphere and held by a polytetrafluoroethylene O-ring next to polycrystalline gold surface (a 60 nm layer, nominally of Au(111)), with measured root mean square roughness of 0.5 nm over 500 nm

× 500 nm area. The mica Au(111) coated substrate for AFM was obtained from Molecular Imaging and pre-treated according to the published procedure[25]. Standard Si AFM cantilevers (model NSC36, MikroMasch, Sofia, Bulgaria) were used throughout. The surface and cantilever were cleaned by washing with deionized water and absolute ethanol, before drying and irradiating using a UV-Ozone cleaner for 20 minutes prior to use. The electrochemical cell consists of the Au(111)/mica substrate and two 0.25 mm platinum wires (Alfa, 99,99%) as working, quasi-reference, and counter electrode. The potential for redox couple for ferrocene/ferrocenium (Fc/Fc^{+}) was assessed in examined ILs in order to get the quasi-reference electrode potential. The potential of the quasi-reference platinum electrode remained stable during all conducted experiments. The measured spring constant was 1.6 N/m. The potential on the working electrode was applied and maintained by Autolab PGSTAT20 software-controlled potentiostat in a three-electrode configuration. More details on AFM measurements can be found in the Supplementary Information.

Acknowledgements

D.A.R., F.C., M.F., P.C.H., and A.N.S. acknowledge the Australian Research Council (ARC) for funding via the Australian Centre for Electromaterials Science, grant CE140100012. M.F. acknowledge the ARC grant DP160101178. The simulation work was undertaken with the assistance of resources provided at the NCI National Facility systems at the Australian National University through the National Computational Merit Allocation Scheme supported by the Australian Government. D.A.R. would like to thank Dr. Srđan Begić and Dr. Erlendur Jónsson for mentoring in simulation skills.

Author Contributions

M.F. conceived the idea. D.A.R. carried out the MD simulations and analysis under the

supervision of F.C. and M.F., and AFM experiment under the supervision of R.A. and H.L., S.A.F. and T.P. contributed to the electrochemical experiments under the supervision of P.C.H., D.A.R. F.C. and M.F. drafted the manuscript. R.A. and A.N.S. helped in editing the manuscript. All authors contributed to the discussion of results.

Additional information

Supplementary information is available in the online version of the paper.

Reprints and permissions information is available online at www.nature.com/reprints.

Correspondence and requests for materials should be addressed to Maria Forsyth or Fangfang Chen.

Competing financial interests

The authors declare no competing financial interests.

References

1. Fedorov, M. V. & Kornyshev, A. A. Ionic Liquids at Electrified Interfaces. *Chem. Rev.* **114**, 2978–3036 (2014).
2. Xu, K. Electrolytes and interphases in Li-ion batteries and beyond. *Chem. Rev.* **114**, 11503–11618 (2014).
3. Cheng, X. B. *et al.* A review of solid electrolyte interphases on lithium metal anode. *Adv. Sci.* **3**, 1–20 (2015).
4. Lin, D., Liu, Y. & Cui, Y. Reviving the lithium metal anode for high-energy batteries. *Nat. Nanotechnol.* **12**, 194–206 (2017).
5. Cheng, X. B., Zhang, R., Zhao, C. Z. & Zhang, Q. Toward Safe Lithium Metal Anode in Rechargeable Batteries: A Review. *Chem. Rev.* **117**, 10403–10473 (2017).
6. Lee, B., Paek, E., Mitlin, D. & Lee, S. W. Sodium Metal Anodes: Emerging Solutions to Dendrite Growth. *Chem. Rev.* **119**, 5416–5460 (2019).
7. Watanabe, M. *et al.* Application of Ionic Liquids to Energy Storage and Conversion Materials and Devices. *Chem. Rev.* **117**, 7190–7239 (2017).
8. Mezger, M. *et al.* Molecular Layering of Fluorinated Lonic Liquids at a Charged

Sapphire (0001) Surface. *Science (80-.).* **322**, 424–428 (2008).

9. Mao, X. *et al.* Self-assembled nanostructures in ionic liquids facilitate charge storage at electrified interfaces. *Nat. Mater.* **18**, 1350–1357 (2019).
10. Black, J. M. *et al.* Fundamental aspects of electric double layer force-distance measurements at liquid-solid interfaces using atomic force microscopy. *Sci. Rep.* **6**, 1–12 (2016).
11. Black, J. M. *et al.* Bias-dependent molecular-level structure of electrical double layer in ionic liquid on graphite. *Nano Lett.* **13**, 5954–5960 (2013).
12. Smith, A. M., Lee, A. A. & Perkin, S. The Electrostatic Screening Length in Concentrated Electrolytes Increases with Concentration. *J. Phys. Chem. Lett.* **7**, 2157–2163 (2016).
13. Su, Y.-Z., Fu, Y.-C., Yan, J.-W., Chen, Z.-B. & Mao, B.-W. Double Layer of Au(100)/Ionic Liquid Interface and Its Stability in Imidazolium-Based Ionic Liquids. *Angew. Chemie Int. Ed.* **48**, 5148–5151 (2009).
14. Elbourne, A. *et al.* Nanostructure of the Ionic Liquid-Graphite Stern Layer. *ACS Nano* **9**, 7608–7620 (2015).
15. Motobayashi, K., Minami, K., Nishi, N., Sakka, T. & Osawa, M. Hysteresis of potential-dependent changes in ion density and structure of an ionic liquid on a gold electrode: In situ observation by surface-enhanced infrared absorption spectroscopy. *J. Phys. Chem. Lett.* **4**, 3110–3114 (2013).
16. Nanbu, N., Sasaki, Y. & Kitamura, F. In situ FT-IR spectroscopic observation of a room-temperature molten salt|gold electrode interphase. *Electrochem. commun.* **5**, 383–387 (2003).
17. Rubim, J. C., Trindade, F. A., Gelesky, M. A., Aroca, R. F. & Dupont, J. Surface-Enhanced Vibrational Spectroscopy of Tetrafluoroborate 1-n-Butyl-3-methylimidazolium (BMIBF4) Ionic Liquid on Silver Surfaces. *J. Phys. Chem. C* **112**, 19670–19675 (2008).
18. Yuan, Y.-X., Niu, T.-C., Xu, M.-M., Yao, J.-L. & Gu, R.-A. Probing the adsorption of methylimidazole at ionic liquids/Cu electrode interface by surface-enhanced Raman scattering spectroscopy. *J. Raman Spectrosc.* **41**, 516–523 (2010).
19. Baldelli, S. Surface structure at the ionic liquid-electrified metal interface. *Acc. Chem. Res.* **41**, 421–431 (2008).
20. Hu, Z., Vatamanu, J., Borodin, O. & Bedrov, D. A molecular dynamics simulation study of the electric double layer and capacitance of [BMIM][PF6] and [BMIM][BF4] room

temperature ionic liquids near charged surfaces. *Phys. Chem. Chem. Phys.* **15**, 14234–14247 (2013).

21. Begić, S., Li, H., Atkin, R., Hollenkamp, A. F. & Howlett, P. C. A comparative AFM study of the interfacial nanostructure in imidazolium or pyrrolidinium ionic liquid electrolytes for zinc electrochemical systems. *Phys. Chem. Chem. Phys.* **18**, 29337–29347 (2016).
22. Forsyth, M. *et al.* Tuning Sodium Interfacial Chemistry with Mixed-Anion Ionic Liquid Electrolytes. *ACS Appl. Mater. Interfaces* (2019). doi:10.1021/acsami.9b12913
23. Liu, Z. *et al.* Dendrite-Free Nanocrystalline Zinc Electrodeposition from an Ionic Liquid Containing Nickel Triflate for Rechargeable Zn-Based Batteries. *Angew. Chemie - Int. Ed.* **55**, 2889–2893 (2016).
24. Li, H., Endres, F. & Atkin, R. Effect of alkyl chain length and anion species on the interfacial nanostructure of ionic liquids at the Au(111)-ionic liquid interface as a function of potential. *Phys. Chem. Chem. Phys.* **15**, 14624–14633 (2013).
25. Atkin, R. *et al.* AFM and STM studies on the surface interaction of [BMP]TFSA and [EMIm]TFSA ionic liquids with Au(111). *J. Phys. Chem. C* **113**, 13266–13272 (2009).
26. Carstens, T., Lahiri, A., Borisenko, N. & Endres, F. [Py1,4]-FSI-NaFSI-based ionic liquid electrolyte for sodium batteries: Na+ solvation and interfacial nanostructure on Au(111). *J. Phys. Chem. C* **120**, 14736–14741 (2016).
27. Hoffmann, V. *et al.* Influence of a silver salt on the nanostructure of a Au(111)/ionic liquid interface: An atomic force microscopy study and theoretical concepts. *Phys. Chem. Chem. Phys.* **20**, 4760–4771 (2018).
28. Lahiri, A., Carstens, T., Atkin, R., Borisenko, N. & Endres, F. In Situ Atomic Force Microscopic Studies of the Interfacial Multilayer Nanostructure of LiTFSI-[Py1, 4]TFSI on Au(111): Influence of Li+ Ion Concentration on the Au(111)/IL Interface. *J. Phys. Chem. C* **119**, 16734–16742 (2015).
29. Girard, G. M. A. *et al.* Spectroscopic Characterization of the SEI Layer Formed on Lithium Metal Electrodes in Phosphonium Bis(fluorosulfonyl)imide Ionic Liquid Electrolytes. *ACS Appl. Mater. Interfaces* **10**, 6719–6729 (2018).
30. Yoon, H., Howlett, P. C., Best, A. S., Forsyth, M. & MacFarlane, D. R. Fast charge/discharge of Li metal batteries using an ionic liquid electrolyte. *J. Electrochem. Soc.* **160**, 1629–1637 (2013).
31. Forsyth, M. *et al.* Novel Na+ Ion Diffusion Mechanism in Mixed Organic-Inorganic Ionic Liquid Electrolyte Leading to High Na+ Transference Number and Stable, High

Rate Electrochemical Cycling of Sodium Cells. *J. Phys. Chem. C* **120**, 4276–4286 (2016).

32. Zhang, H. *et al.* Ionic liquid electrolyte with highly concentrated LiTFSI for lithium metal batteries. *Electrochim. Acta* **285**, 78–85 (2018).
33. Choudhury, S. *et al.* Designing solid-liquid interphases for sodium batteries. *Nat. Commun.* **8**, 1–10 (2017).
34. Periyapperuma, K. *et al.* Towards high rate Li metal anodes: Enhanced performance at high current density in a superconcentrated ionic liquid. *J. Mater. Chem. A* (2019). doi:10.1039/C9TA12004A
35. Wakeham, D., Nelson, A., Warr, G. G. & Atkin, R. Probing the protic ionic liquid surface using X-ray reflectivity. *Phys. Chem. Chem. Phys.* **13**, 20828–20835 (2011).
36. Chen, F., Howlett, P. & Forsyth, M. Na-Ion Solvation and High Transference Number in Superconcentrated Ionic Liquid Electrolytes: A Theoretical Approach. *J. Phys. Chem. C* **122**, 105–114 (2018).
37. Haskins, J. B., Bauschlicher, C. W. & Lawson, J. W. Ab Initio Simulations and Electronic Structure of Lithium-Doped Ionic Liquids: Structure, Transport, and Electrochemical Stability. *J. Phys. Chem. B* **119**, 14705–14719 (2015).
38. Matsumoto, K., Okamoto, Y., Nohira, T. & Hagiwara, R. Thermal and transport properties of Na[N(SO2F)2]-[N-Methyl-N-propylpyrrolidinium][N(SO2F)2] ionic liquids for Na secondary batteries. *J. Phys. Chem. C* **119**, 7648–7655 (2015).
39. Vicent-Luna, J. M. *et al.* Quantum and Classical Molecular Dynamics of Ionic Liquid Electrolytes for Na/Li-based Batteries: Molecular Origins of the Conductivity Behavior. *ChemPhysChem* 2473–2481 (2016). doi:10.1002/cphc.201600285
40. Giffin, G. A., Moretti, A., Jeong, S. & Passerini, S. Decoupling effective Li+ion conductivity from electrolyte viscosity for improved room-temperature cell performance. *J. Power Sources* **342**, 335–341 (2017).
41. Gao, X., Wu, F., Mariani, A. & Passerini, S. Concentrated Ionic-Liquid-Based Electrolytes for High-Voltage Lithium Batteries with Improved Performance at Room Temperature. *ChemSusChem* **12**, 4185–4193 (2019).
42. Wróbel, P., Kubisiak, P. & Eilmes, A. Interactions in Sodium Bis(fluorosulfonyl)imide/1-Ethyl-3-methylimidazolium Bis(fluorosulfonyl)imide Electrolytes for Na-Ion Batteries: Insights from Molecular Dynamics Simulations. *J. Phys. Chem. C* **123**, 14885–14894 (2019).
43. Tsuzuki, S., Hayamizu, K. & Seki, S. Origin of the low-viscosity of [emim][(FSO2)2N]

ionic liquid and its lithium salt mixture: Experimental and theoretical study of self-diffusion coefficients, conductivities, and intermolecular interactions. *J. Phys. Chem. B* **114**, 16329–16336 (2010).

44. Takenaka, N. *et al.* Microscopic Formation Mechanism of Solid Electrolyte Interphase Film in Lithium-Ion Batteries with Highly Concentrated Electrolyte. *J. Phys. Chem. C* **122**, 2564–2571 (2018).
45. Makhlooghiazad, F. *et al.* Phosphonium plastic crystal salt alloyed with a sodium salt as a solid-state electrolyte for sodium devices: phase behaviour and electrochemical performance. *J. Mater. Chem. A* **5**, 5770–5780 (2017).
46. Lindahl, E., Hess, B. & van der Spoel, D. GROMACS 3.0: a package for molecular simulation and trajectory analysis. *Mol. Model. Annu.* **7**, 306–317 (2001).
47. Wang, R., Bi, S., Presser, V. & Feng, G. Systematic comparison of force fields for molecular dynamic simulation of Au(111)/Ionic liquid interfaces. *Fluid Phase Equilib.* **463**, 106–113 (2018).
48. Vatamanu, J., Xing, L., Li, W. & Bedrov, D. Influence of temperature on the capacitance of ionic liquid electrolytes on charged surfaces. *Phys. Chem. Chem. Phys.* **16**, 5174–5182 (2014).